Acoustic circular dichroism in a three-dimensional chiral metamaterial

Qing Tong [1], Jensen Li [2], and Shubo Wang [1,*]

[1]*Department of Physics, City University of Hong Kong, Tat Chee Avenue, Kowloon, Hong Kong, China*

[2]*Department of Physics, The Hong Kong University of Science and Technology, Kowloon, Hong Kong, China*

(Received 6 January 2023; revised 24 March 2023; accepted 27 March 2023; published 5 April 2023)

Circular dichroism (CD) is an intriguing chiroptical phenomenon associated with the interaction of chiral structures with circularly polarized lights. Although the CD effect has been extensively studied in optics, it has not yet been demonstrated in acoustic systems. Here, we demonstrate the acoustic CD effect in a three-dimensional chiral metamaterial supporting circularly polarized transverse sound. We find that the effect is negligible in the lossy metamaterial possessing C_4 rotational symmetry but can be strongly enhanced in the C_2-symmetric system with inhomogeneous loss. The phenomena can be understood based on the properties of the metamaterial's complex band structure and the quality factors of its eigenmodes. We show that the enhanced CD in the C_2-symmetric system is attributed to the polarization band gaps and the non-Hermitian exceptional points appearing near the Brillouin-zone center and boundaries. The results contribute to the understanding of chiral sound-matter interactions and can find applications in acoustic sensing of chiral structures and sound manipulations based on vector properties.

DOI: 10.1103/PhysRevB.107.134103

I. INTRODUCTION

Chiral structures have novel properties deriving from mirror-symmetry breaking [1,2] and are extensively employed to realize polarization conversion [3,4], unusual optical forces [5–7], and synthetic gauge fields [8]. The interaction between chiral structures and chiral light, i.e., light carrying spin and/or orbital angular momentum (OAM), can give rise to circular dichroism (CD) [2,9,10] and helical (or vortical) dichroism [11,12], corresponding to the differential absorption of lights with opposite chirality. The CD effect has been investigated in various optical structures, ranging from bilayer chiral structures [13,14] and nonplanar three-dimensional (3D) chiral structures [15] to gyroid structures [16,17]. Recent research has uncovered the subtle relations between CD and the Ohmic dissipation of metaatoms [18] as well as the bound states in the continuum [19], enabling a profound understanding of chiral light-matter interactions. The CD effect has been widely applied to analyze molecular structures [20,21] and to achieve chiral discrimination [22,23].

It is well known that sound can carry OAM in the form of vortices [24–26]. The acoustic OAM can induce chiral sound-matter interactions and give rise to intriguing phenomena such as acoustic geometric phases [27] and the acoustic orbital Hall effect [28,29]. The chiral sound-matter interactions can enable rich manipulations of sound vortices, including asymmetric transmission and reflection [30], reversal of orbital angular momentum [31], and acoustic helical dichroism [32]. In addition, the chiral sound-matter interactions can be applied to manipulate matter, leading to acoustic levitation [33,34], acoustic tweezers [35–37], and acoustic torque [38,39]. Here and in what follows, the sound corresponds to the acoustic wave propagating through air. While the sound propagating through solids (i.e., elastic wave) supports both transverse and longitudinal modes, the conventional airborne sound is a longitudinal wave. Recently, it was shown that inhomogeneous sound fields can carry nonzero acoustic spin density characterized by rotating velocity vector fields [40,41]. Remarkably, spin-1 transverse sound can emerge in a micropolar metamaterial supporting synthetic shear forces in air [42]. In contrast to the conventional longitudinal sound, the transverse sound carries full vector properties similar to electromagnetic waves and is characterized by a dispersion relation with nonzero frequency at wave number $k = 0$. In particular, it can carry both spin and OAM with intriguing spin-orbit interactions. Exploration of this new type of sound and its counterintuitive properties can generate new functionalities for acoustic applications.

Here we demonstrate the acoustic CD effect in a 3D chiral metamaterial that supports circularly polarized transverse sound. Using full-wave numerical simulations, we calculate the absorption of left-handed circularly polarized (LCP) and right-handed circularly polarized (RCP) sound in the lossy metamaterial. We find that the CD effect strongly depends on the rotational symmetry of the metamaterial. The CD effect is negligible in the metamaterial with homogeneous loss satisfying the C_4 rotational symmetry. In contrast, it is strongly enhanced in the metamaterial with inhomogeneous loss satisfying the C_2 rotational symmetry. By studying the complex band structure of the metamaterial and the quality factors of its eigenmodes, we find that these properties originate from the polarization band gaps and the non-Hermitian exceptional points (EPs) of the metamaterial.

We organize the article as follows. In Sec. II, we introduce the acoustic chiral metamaterial and discuss its eigenmode properties. In Sec. III, we show the numerical results for the absorption of the LCP and RCP sound in two types of lossy metamaterial obeying the C_4 and C_2 rotational symmetry,

*shubwang@cityu.edu.hk

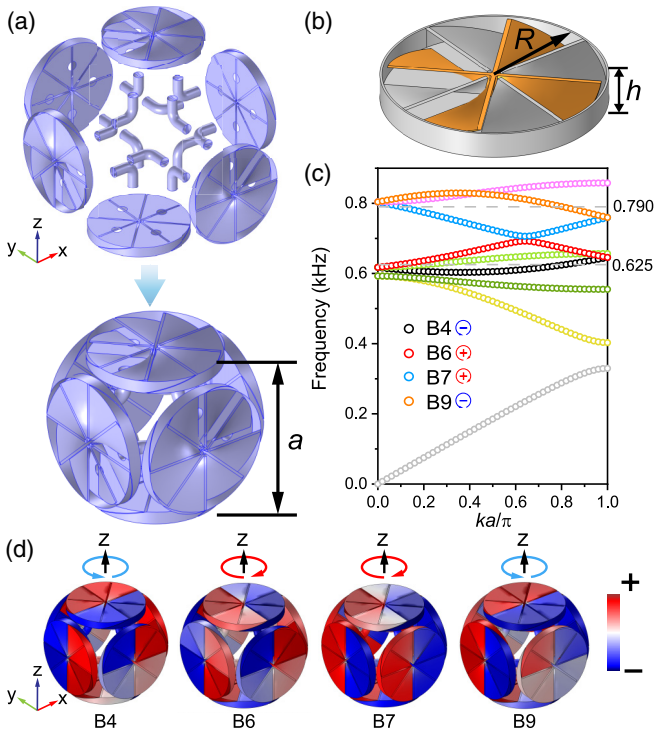

FIG. 1. (a) Unit cell of the 3D acoustic metamaterial. (b) Internal structure of the resonators. The geometry parameters are $R = 5$ cm, $h = 1$ cm, $a = 12.1$ cm. (c) Band structure of the metamaterial. B4, B6, B7, and B9 denote the lowest four bands with circularly polarized eigenstates. (d) Pressure fields at $ka/\pi = 0.2$ for B4, B6, B7, and B9. The blue and red arrows denote the circulating direction of the eigen pressure fields for the LCP and RCP states, respectively.

respectively. Section IV presents the complex band structures of the lossy metamaterials, where we discuss the polarization band gaps and the EPs to understand the CD effect. We draw the conclusion in Sec. V.

II. THE CHIRAL METAMATERIAL

We consider a 3D metamaterial with the cubical unit cell shown in Fig. 1(a). The unit cell comprises three chiral resonators mutually connected by tubes, and it obeys the C_4 rotational symmetry with respect to the x, y, and z axes. Figure 1(b) shows a half of the chiral resonator, where the radius is $R = 5$ cm and the height is $h = 1$ cm. The orange blades are connected to the center post, and the gray blades are connected to the outer shell of the resonator. We assume that air is filled inside the resonator and all air-material interfaces are hard boundaries. In the considered range of frequencies, each resonator supports subwavelength resonances. These resonances endow the metamaterial with intriguing macroscopic acoustic properties.

We first calculate the band structure of the metamaterial by using a finite-element package COMSOL MULTIPHYSICS. The result is shown in Fig. 1(c) for the wave vector in the z direction. The fourth to ninth bands (counting from bottom) correspond to the eigenmodes dominated by the dipole resonances of the chiral resonators. Here, we focus on the bands labeled as B4, B6, B7, and B9. The eigenmodes of

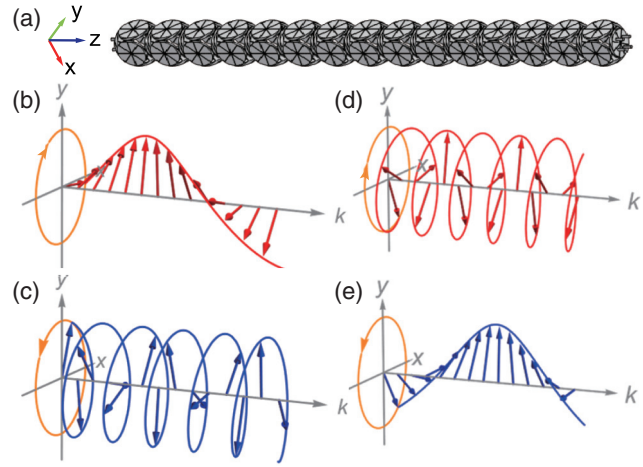

FIG. 2. (a) The metamaterial with 15 units in z direction and periodic in x and y directions. The transverse sound is excited by ports on the left end of the metamaterial. (b)–(e) Averaged velocity vectors in the metamaterial at the frequency $f = 0.625$ kHz (b and c) and 0.79 kHz (d and e). The yellow circles with the arrow show the circulating direction of the velocity field on the xy plane.

these bands are circularly polarized transverse sound [42], and their pressure fields are shown in Fig. 1(d) for $ka/\pi = 0.2$. As seen, the fields represent acoustic dipoles oscillating in a direction perpendicular to the axis of the resonators. The arrowed circles denote the rotation direction of the eigenfields. The red and blue arrowed circles correspond to the RCP states and LCP states, respectively. The velocity field averaged over the unit cell also circulates in the same direction. The collective motion of the acoustic dipoles gives rise to circularly polarized transverse sound macroscopically. The transverse sound of the bands B4 and B6 (B7 and B9) have opposite handedness and carry opposite spin angular momentum.

To demonstrate the emergence of circularly polarized transverse sound, we consider the metamaterial with 15 unit cells in the z direction, as shown in Fig. 2(a). Periodic boundary conditions are applied in the x and y directions. To excite the system, we set four input ports at the four tubes on the left side of the unit in Fig. 2(a) with the phases 0, 0.5π, π, and 1.5π, respectively. The azimuthal gradient of the phase decides the handedness (LCP or RCP) of the excited circularly polarized transverse sound. In addition, we set another four output ports on the right side of the metamaterial to determine the transmission. We consider two frequencies, 0.625 and 0.79 kHz, corresponding to the frequencies marked by the dashed lines in Fig. 1(c), where four eigenstates (two are of LCP and two are of RCP) can be excited. To visualize the transverse sounds, we average the velocity field over each unit cell and plot the averaged velocity vectors (denoted by the red and blue arrows) for the 15 unit cells in Figs. 2(b)–2(e). We observe that the velocity vectors indeed rotate in the xy plane, corresponding to spin angular momentum in the longitudinal direction (i.e., z direction). The arrowed yellow circles denote the temporal evolution of the velocity vectors, with the arrows indicating the circulation direction. At either frequency, the two transverse sounds carry opposite spins, allowing the exploration of their different absorption inside the metamaterial.

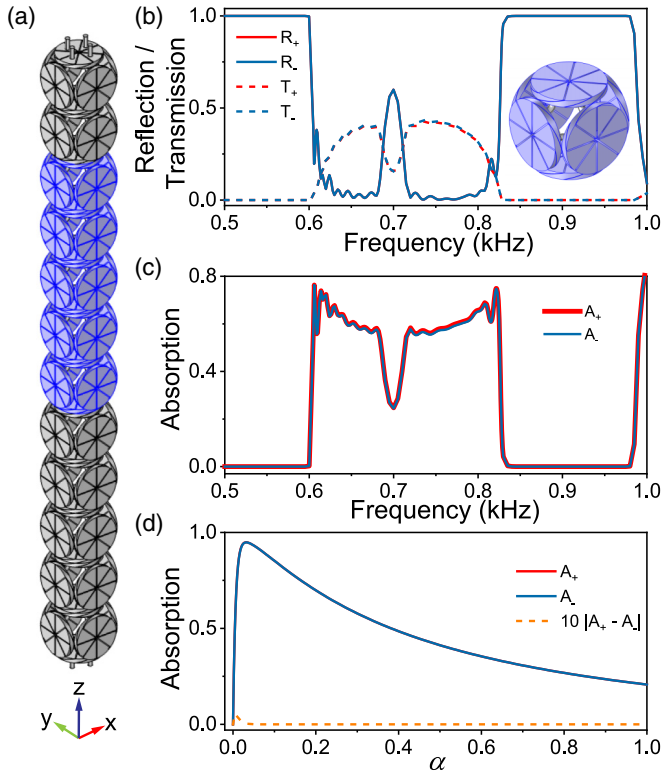

FIG. 3. (a) The three-layer metamaterial with loss uniformly added to the middle layer (colored in blue). (b) Reflection, transmission, and (c) absorption as a function of frequency for the RCP (+) and LCP (−) sounds with $\alpha = 0.006$. The inset in (b) shows the regions containing loss (blue colored), which satisfies the C_4 symmetry. (d) Absorption of the LCP and RCP sounds as a function of the loss α at 0.65 kHz. In (c) and (d), the absorption difference (ΔA) is multiplied by ten for easy visualization.

III. ACOUSTIC CIRCULAR DICHROISM

We now consider the metamaterial with loss to investigate the CD effect of the transverse sound. As shown in Fig. 3(a), we employ a three-layer sandwich structure: the bottom and top layers are lossless, while the middle layer (highlighted in blue) contains loss. The loss is introduced into the unit cells by adding an imaginary part to the sound speed $v(1 + i\alpha)$ with α characterizing the loss strength, which is a common way to simulate loss in acoustic systems [43,44]. We apply ports to excite the system (same as in Fig. 2) from the bottom of the lattice. The excited transverse sound propagates through the middle lossy layer and is measured in the top layer to determine its transmission. This directly maps to the usual configuration of optical CD, where an optical structure is sandwiched by air and reflection/transmission is measured in air. We apply COMSOL to simulate the system and calculate the reflection ($R_\pm$) and transmission ($T_\pm$) of the incident sound. The absorptions can then be determined as

$$A_\pm = 1 - R_\pm - T_\pm, \tag{1}$$

$$\Delta A = |A_+ - A_-|, \tag{2}$$

where "+" ("−") denotes the RCP (LCP) state and ΔA is the differential absorption of the RCP and LCP sounds.

We first consider the case with loss uniformly added to all the chiral resonators in the middle blue-colored layer. Figure 3(b) shows the numerical results of the reflections (solid lines) and transmissions (dashed lines). The inset shows the unit cell with the blue-colored regions containing loss $\alpha = 0.006$, which has C_4 rotational symmetry. As seen, the reflection R_+ is nearly identical to R_-, and there is a tiny difference between the transmissions T_+ and T_-. The absorptions calculated using Eq. (1) are shown in Fig. 3(c) as the solid blue and red lines. We notice that the absorptions of LCP and RCP sounds are almost equal. As a result, the CD effect is negligible in this case with homogeneous loss. Figure 3(d) shows the absorption of the LCP and RCP sound as a function of the loss strength α at $f = 0.65$ kHz. We notice that the absorption A_+ and A_- are almost identical. The differential absorption ΔA is less than 0.01 with the maximum appearing at $\alpha = 0.006$, as shown by the orange dashed line, which has been multiplied by a factor of 10.

The optical CD effect strongly depends on the rotational symmetry of the structures [45,46]. To explore this symmetry dependence for acoustic CD, we break the C_4 symmetry of the metamaterial by selectively adding loss to the unit cells. As shown in the inset of Fig. 4(a), we only add loss to the side resonator (i.e., two opposing half resonators highlighted in blue) with the center axis in the x direction, reducing the symmetry of the metamaterial from C_4 to C_2. We numerically calculated the transmission and reflection of this C_2 system, and the results are shown in Fig. 4(a) for loss $\alpha = 0.1$. We observe large differences in the transmissions and reflections of the LCP and RCP sound in the frequency range [0.600 kHz, 0.825 kHz], corresponding to the considered bands in Fig. 1(c). The absorptions calculated with Eq. (1) are shown in Fig. 4(b). As noticed, there is a significant difference between the absorption of RCP sound (A_+) and the absorption of RCP sound (A_-). The differential absorption ΔA (denoted by the orange dashed line) is much larger than the case of Fig. 3 and has two local maxima of about 0.5 appearing at 0.65 and 0.80 kHz. This demonstrates the strong CD phenomena in the C_2 metamaterial. We also investigate the dependence of the CD on the loss magnitude α, and the results are shown in Fig. 4(c) for $f = 0.65$ kHz. The trends of A_+ and A_- are similar to those of the C_4 system, but the absorption difference ΔA (denoted by the dashed orange line) is much larger with a maximum value of 0.46 at $\alpha = 0.3$ (marked by the dashed line).

The CD characterizes the different absorption of LCP and RCP sounds at the same frequency. We note that the LCP and RCP sounds have different wavelengths inside the chiral metamaterial at the same frequency due to their different dispersions. It is thus interesting to compare their absorption for the same wavelength (or wave number) inside the metamaterial. Figure 4(d) shows the absorption of the transverse sound corresponding to the four bands B4, B6, B7, and B9 in Fig. 1(c). We only consider the range of $0 \leqslant ka/\pi \leqslant 0.2$ where the effective wavelength is well defined, and the excited state is RCP for band B4 and LCP for band B7 due to their negative group velocity in this range. As seen, the RCP sounds (corresponding to the solid and dashed red lines) generally have larger absorption compared with the LCP sounds (corresponding to the solid and dashed blue lines). This indicates

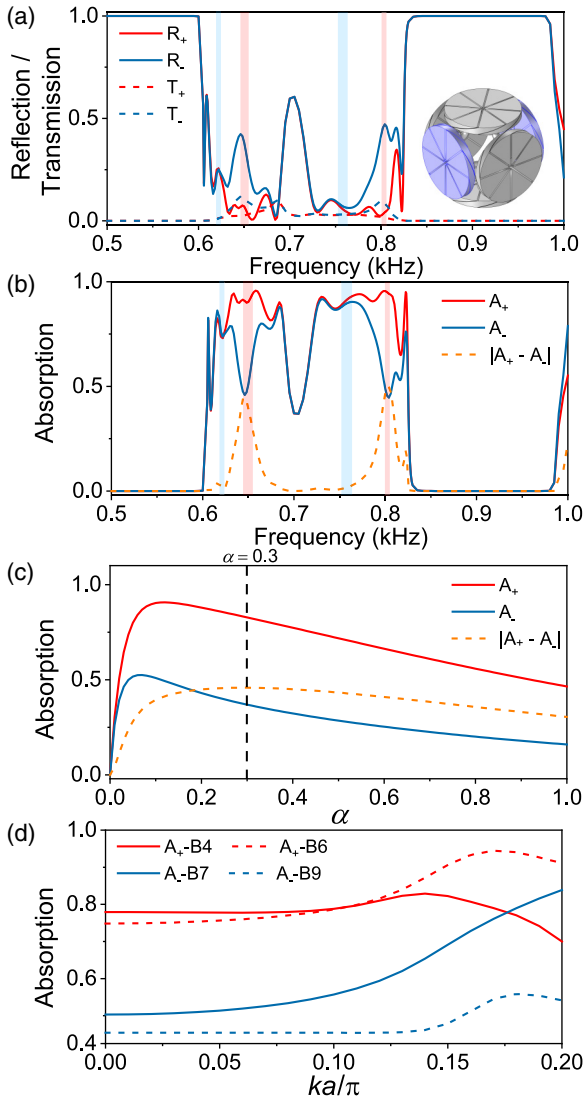

FIG. 4. (a) Reflection, transmission, and (b) absorption of the RCP (+) and LCP (−) sounds for $\alpha = 0.1$. The inset in (a) shows the regions with loss (blue colored), which satisfies the C_2 symmetry. (c) Absorption of the LCP and RCP sounds as a function of the loss parameter α at 0.65 kHz. (d) Absorption of the LCP and RCP sounds as a function of the normalized wave number ka/π for the bands B4, B6, B7, and B9.

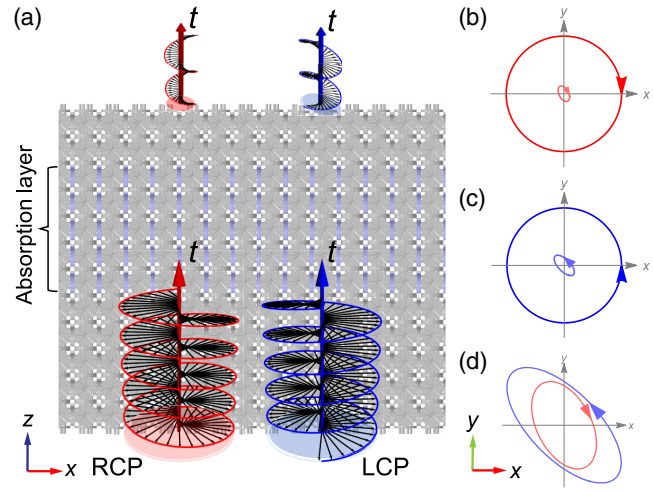

FIG. 5. (a) Schematics of the CD effect in the acoustic metamaterial. The red and blue helical curves denote the temporal trajectories of the velocity vectors for the RCP and LCP sounds on the incident side (bottom) and the transmission side (top). (b and c) Larger (smaller) circles denote the evolution trajectories of velocity field for the incident (transmitted) RCP and LCP sounds. The transmitted sounds are elliptically polarized. (d) A zoom-in comparison of the transmitted velocity field's trajectories under the incidence of RCP (red) and LCP (blue) sound. We set the frequency $f = 0.635$ kHz and loss $\alpha = 0.1$.

that a strong CD effect also happens to the circularly polarized transverse sounds with the same wavelength (but not necessarily the same frequency).

To intuitively understand the different absorption of LCP and RCP sounds, we then study the averaged velocity fields (averaged over one unit cell) in the three-layer metamaterial with C_2 symmetry. Figure 5(a) shows a side view of the metamaterial, where loss is added to the middle layers consisting of five unit cells (the blue color marks the resonators containing loss). The red and blue helical curves in the bottom layer denote the temporal trajectories of the velocity vectors of the incident RCP and LCP sounds, respectively. The helical curves in the upper layer denote the temporal trajectories of the velocity vectors of the transmitted sounds, which are in general elliptically polarized due to the coupling between the LCP and RCP sounds in the C_2 absorptive layer. Figures 5(b) and 5(c) show the numerical results of the transmitted velocity fields under the incidence of the RCP and LCP sounds, respectively, for $f = 0.635$ kHz and $\alpha = 0.1$. The larger arrowed circles denote the time-evolution trajectories of the incident velocity fields, while the smaller ellipses denote the time-evolution trajectories of the transmitted velocity fields. Figure 5(d) shows a comparison between the transmitted velocity fields under the incidence of LCP and RCP sounds [corresponding to a zoom-in of the results in Figs. 5(b) and 5(c)], which are different in both amplitude and ellipticity. A similar property also exists in the reflected fields.

IV. COMPLEX BAND STRUCTURE AND EXCEPTIONAL POINTS

We investigate the complex band structures of the systems to uncover the origins of the acoustic CD and the different properties of the C_2 and C_4 systems. Figures 6(a) and 6(b) show the real and imaginary parts of the complex band structure for the C_4 system with loss $\alpha = 0.006$ (corresponding to the case of Fig. 3). The imaginary parts take positive values due to the time convention $e^{i\omega t}$ adopted in COMSOL. The insets (labeled as A, B, C, and D) on the right side show the zoom-ins of the bands enclosed by the dashed rectangles. The insets A and B depict the bands near the Brillouin zone centers and boundaries, respectively, for B4 and B6. Likewise, insets C and D show the bands closed to the Brillouin zone centers and boundaries, respectively, for B7 and B9. We notice that the band degeneracies are not affected by the loss due to the protection of the C_4 symmetry.

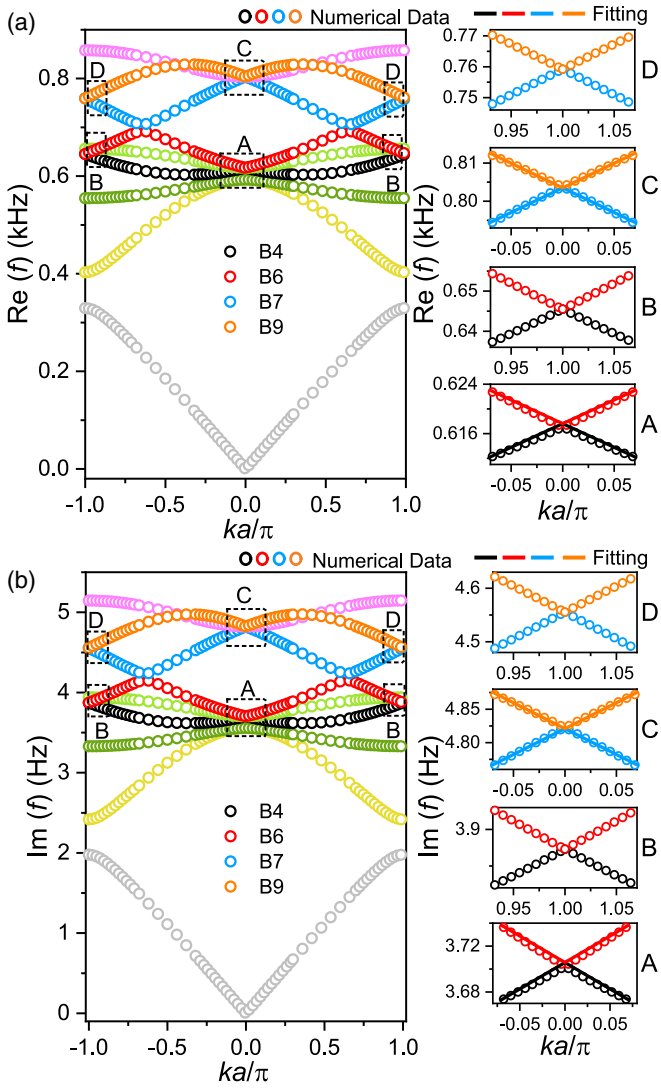

FIG. 6. The (a) real and (b) imaginary parts of the complex band structure for the C_4 system at $\alpha = 0.006$. Insets on the right side show the zoom-ins of the bands near the zone center and boundaries, corresponding to the dashed rectangles in (a) and (b). The solid lines in the insets denote the analytical fitting results.

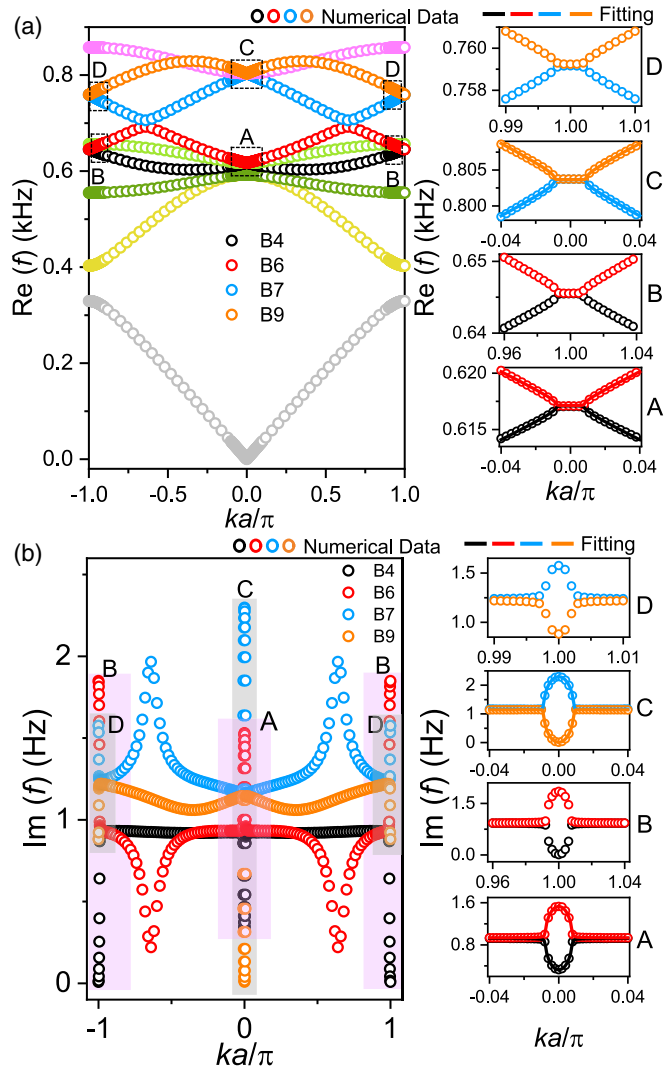

FIG. 7. The (a) real and (b) imaginary parts of complex band structure for the C_2 system at $\alpha = 0.006$. The insets on the right side show the zoom-ins of the bands near the zone center and boundaries, corresponding to the dashed rectangles in (a) and shaded rectangles in (b). The solid lines in the insets denote the analytical fitting results.

Figure 7 shows the complex band structure for the C_2 system with the same loss $\alpha = 0.006$ for comparison with the C_4 system. Interestingly, at the Brillouin zone center and boundaries, the real parts of the bands remain degenerate in a finite range of k values while the imaginary parts bifurcate in the same range, as shown in the insets on the right side. This indicates the emergence of non-Hermitian exceptional points [47–49]. Obviously, these EPs derive from the diabolic points of the original lossless system in Fig. 1(c). While the phenomena here is similar to the EPs spawn from Dirac points in two-dimensional photonic crystals [47], the underlying physical mechanism is different. The emergence of these EPs is attributed to the coupling and loss difference of the LCP and RCP transverse dipole modes induced by the breaking of C_4 symmetry. We will elaborate on this point with an analytical model later.

Figures 8(a) and 8(b) show the complex band structure for the C_2 system with a larger loss $\alpha = 0.1$, corresponding to the case of Figs. 4(a) and 4(b) with a much stronger CD effect. We notice that the EP features remain at the center and boundaries of the Brillouin zone. At the same time, small partial gaps appear at the frequencies of the EPs, as marked by the blue and red ribbons in the insets of Fig. 8(a). At the frequencies of the blue-ribbon (red-ribbon) region, only LCP (RCP) sound can propagate through the metamaterial [16,49]. Thus, at the frequencies $f = 0.62$ kHz and $f = 0.76$ kHz, the RCP sound cannot propagate through the metamaterial. Similarly, at the frequencies of $f = 0.65$ kHz and $f = 0.80$ kHz, the LCP sound cannot propagate through the metamaterial. However, this does not necessarily indicate a large difference in the reflection of LCP and RCP sounds at these frequencies due to the non-Hermitian nature of the metamaterial. Whether strong reflection will appear at the partial polarization gaps depends on the damping of the corresponding eigenmodes. In

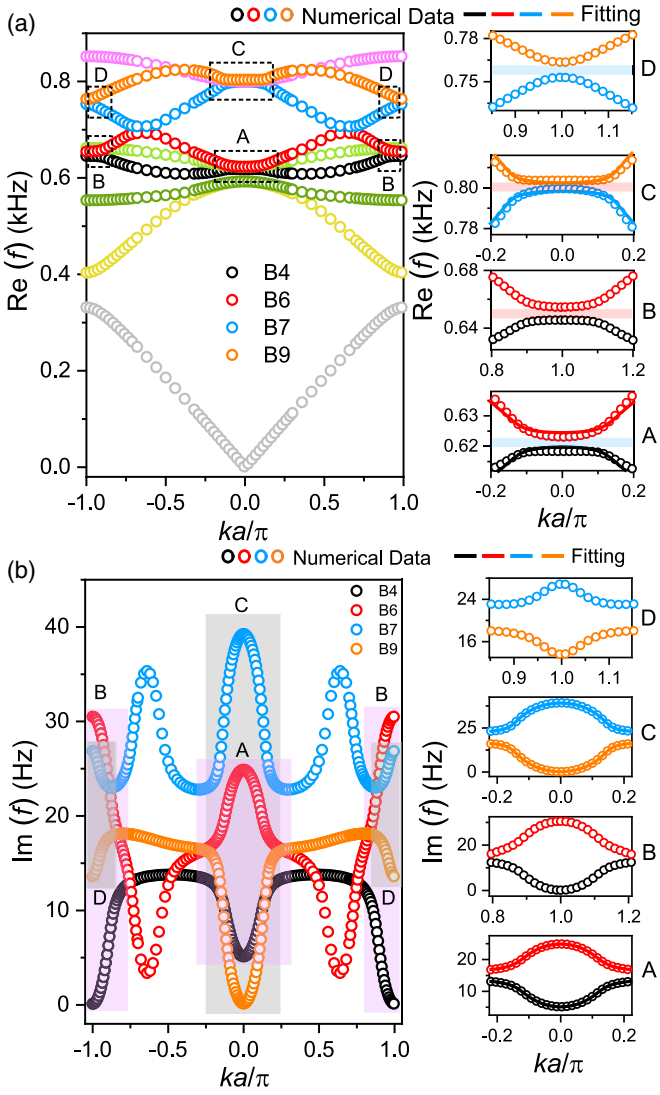

FIG. 8. The (a) real and (b) imaginary parts of complex band structures for the C_2 system at $\alpha = 0.1$. The right insets show the zoom-ins of the bands near the Brillouin zone centers and boundaries, corresponding to the dashed rectangles in (a) and shaded rectangles in (b). The ribbons in the insets denote the partial band gaps. The solid lines in the insets denote the analytical fitting results.

the following, we will show that the eigenmodes' damping property strongly affects the reflection and the CD effect.

To understand the damping of the eigenmodes, we investigate the modes' quality factor Q corresponding to the bands B4, B6, B7, and B9, for both the C_4 and C_2 systems. The quality factor is calculated as $Q = \frac{\mathrm{Re}(f)}{2\mathrm{Im}(f)}$ [50]. The results are shown in Figs. 9(a) and 9(b) as a function of the real part of the eigenfrequency. We note that the eigenmode of each band can be either LCP or RCP, depending on the sign of its group velocity with respect to the phase velocity. Consequently, the quality factor Q of each band can be divided into two parts for the LCP $(-)$ and RCP $(+)$ states, respectively. As shown in Fig. 9(a), all eigenmodes of the C_4 system have approximately the same quality factor. This explains the negligible CD effect in the C_4 system with homogenous loss. In contrast, the quality factors of the LCP and RCP modes in the C_2

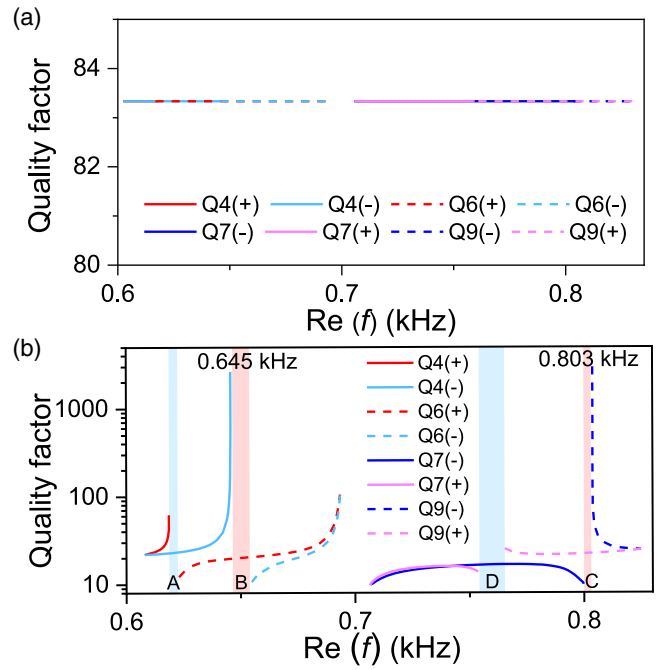

FIG. 9. The quality factor Q of the eigenmodes in the (a) C_4 and (b) C_2 systems, corresponding to the cases of Figs. 6 and 8, respectively. The blue and red ribbons denote polarization band gaps.

system have a large difference, particularly in the vicinity of the polarization band gaps marked by the red ribbons. The large difference in quality factor indicates a large difference in the damping of LCP and RCP modes and thus explains the strong CD effect near the polarization band gaps, in agreement with the numerical results in Fig. 4(b). For the LCP and RCP modes near the blue-ribbon band gaps, their quality factors are much smaller than the modes near the red-ribbon bands, and the difference of their quality factors are also much smaller. Therefore, both LCP and RCP sounds at the frequencies of the blue-ribbon region are strongly absorbed, and their reflections are small, leading to a weak CD effect, as confirmed by the numerical results in Fig. 4(b).

To understand the emergence of the EPs in the C_2 system, we exploit an effective Hamiltonian to describe the coupling of the LCP and RCP modes near the Brillouin zone center [47,48,51,52]. As for the C_4 system with homogenous loss, the effective Hamiltonian can be expressed as

$$H_{C_4} = \begin{pmatrix} \omega_0 - i\gamma & (v_R + iv_I)k \\ (v_R + iv_I)k & \omega_0 - i\gamma \end{pmatrix}, \tag{3}$$

which has the complex eigenvalues

$$\omega = \omega_0 - i\gamma \pm k(v_R + iv_I). \tag{4}$$

Here, ω_0 is the eigenfrequency at $k = 0$, where the LCP and RCP modes are degenerate; v_R and v_I are the real and the imaginary parts of the complex group velocities, respectively; γ denotes the loss.

In the C_2 system, loss is selectively added to only one resonator in each unit cell. The breaking of C_4 symmetry opens a gap at $k = 0$, which can be characterized by a perturbation term $\delta/2$ in the Hamiltonian. The LCP and RCP modes at

TABLE I. Fitting parameters for C_4 and C_2 systems.

System	α	ω_0	γ	v_R	v_I		Inset
C_4	0.006	617.61	−3.71	2.96	0.018		A (Fig. 6)
		803.5	−4.82	4.97	0.03		C (Fig. 6)
	α	ω_0	γ_1	γ_2	v_R	v_I	δ	Inset
C_2	0.006	617.12	−1.53	−0.33	2.96	0.0011	0.036	A (Fig. 7)
		803.66	−0.01	−2.30	4.99	−0.013	0.0075	C (Fig. 7)
	0.1	622.12	−24.87	−5.13	2.98	0.03	4.77	A (Fig. 8)
		800.40	−0.22	−39.12	4.98	−0.21	4.22	C (Fig. 8)

$k = 0$ now have different loss γ_1 and γ_2 ($\gamma_1 \neq \gamma_2$):

$$H_{C_2} = \begin{pmatrix} \omega_0 - i\gamma_1 + \frac{\delta}{2} & (v_R + iv_I)k \\ (v_R + iv_I)k & \omega_0 - i\gamma_2 - \frac{\delta}{2} \end{pmatrix}, \tag{5}$$

which has the complex eigenvalues

$$\omega = \omega_0 - i\frac{(\gamma_1 + \gamma_2)}{2} \pm \frac{1}{2}\sqrt{[\delta - i(\gamma_1 - \gamma_2)]^2 - 4k^2(v_I - iv_R)^2}. \tag{6}$$

These analytical expressions of the complex eigenvalues in Eqs. (4) and (6) are employed to fit the numerical results for both the real and imaginary parts. The fitting results are shown as solid lines in the insets of Figs. 6–8, accordingly. We notice good quantitative agreements between the analytical and numerical results. In particular, the effective Hamiltonian correctly captures the EP features in the C_2 systems. The fitting parameters for both C_4 and C_2 systems with different losses are summarized in Table I. We note that the mode damping parameters $\gamma_{1,2}$ take negative values due to the time convention $e^{i\omega t}$ adopted in COMSOL.

The above effective Hamiltonians well explain the emergence of the EPs and the enhancement of CD by the EPs. In the C_4 system, the LCP mode of the B4 band and the RCP mode of the B6 band are orthogonal at $k = 0$ with vanished coupling. The damping of the LCP and RCP modes at the same excitation frequency are approximately equal due to homogeneous loss added to all resonators of the unit cell. Thus, their quality factors are almost equal [corresponding to the results in Fig. 9(a)]. In the C_2 system, the inhomogeneous loss breaks the C_4 rotational symmetry and induces coupling between the original LCP and RCP modes at $k = 0$, which gives rise to the polarization band gaps. In addition, the two modes have different dampings due to the inhomogeneous material loss. These together give rise to the EPs and the bifurcation of the imaginary parts of the eigenfrequencies, leading to enlarged damping contrast of the LCP and RCP modes at the same excitation frequency and thus a larger difference in their quality factors [corresponding to the results in Fig. 9(b)]. Therefore, the strong CD effect in the C_2 system is attributed to both the polarization band gaps and the EPs.

V. CONCLUSION

In conclusion, we demonstrate the acoustic CD effect in a 3D chiral metamaterial supporting circularly polarized transverse sound. We have investigated the effect in two types of systems with C_4 and C_2 rotational symmetry, respectively. In the C_4 system with loss homogeneously added to all resonators of the unit cell, we observe a negligible acoustic CD effect. On the other hand, by selectively adding loss to part of the unit cell, reducing the system's rotational symmetry from C_4 to C_2, the CD effect is enhanced strongly. With analysis of their complex band structures and quality factors of the eigenmodes, we uncover that the strong acoustic CD in the C_2 system is attributed to polarization band gaps and the emergence of non-Hermitian EPs. The polarization band gaps induce selective transmission and absorption of the circularly polarized transverse sound with a particular handedness. The EPs give rise to bifurcations of the imaginary parts of the eigen frequencies. These together enhance the CD effect in the C_2 system. The results here contribute to the understanding of chiral sound-matter interactions in metamaterials and phononic crystals.

It will be interesting to experimentally demonstrate the discussed phenomena. The metamaterial structures can be fabricated using 3D printing. Loss can be introduced into the structures by adding porous materials such as sponges. The use of porous materials for sound absorption and attenuation has been thoroughly studied in the literature [53,54]. The transverse sound can be excited by using an array of speakers. The reflection and transmission can be measured with a microphone. The acoustic CD effect can be applied to manipulate transverse sound for high-efficiency acoustic communications, where the full vector properties of transverse sound allow the encoding of more information compared to conventional longitudinal sound. It can also find applications in imaging, sensing, and analyzing chiral particles/structures. There is plenty of room to explore the physics of transverse sound in addition to the CD effect, e.g., the spin-Hall effect of transverse sound at an interface and the parametric instability, extensively studied in mechanical metamaterials [55–57], of acoustic systems involving transverse sound.

ACKNOWLEDGMENTS

The work described in this paper was supported by grants from the Research Grants Council of the Hong Kong Special Administrative Region, China (Grants No. CityU 21302018 and No. C6013-18G).

[1] M. Hentschel, M. Schäferling, X. Duan, H. Giessen, and N. Liu, Chiral plasmonics, Sci. Adv. **3**, e1602735 (2017).

[2] J. Mun, M. Kim, Y. Yang, T. Badloe, J. Ni, Y. Chen, C.-W. Qiu, and J. Rho, Electromagnetic chirality: From fundamentals to nontraditional chiroptical phenomena, Light Sci. Appl. **9**, 139 (2020).

[3] J. K. Gansel, M. Thiel, M. S. Rill, M. Decker, K. Bade, V. Saile, G. von Freymann, S. Linden, and M. Wegener, Gold helix photonic metamaterial as broadband circular polarizer, Science **325**, 1513 (2009).

[4] C. Wu, H. Li, X. Yu, F. Li, H. Chen, and C. T. Chan, Metallic Helix Array as a Broadband Wave Plate, Phys. Rev. Lett. **107**, 177401 (2011).

[5] S. B. Wang and C. T. Chan, Lateral optical force on chiral particles near a surface, Nat. Commun. **5**, 3307 (2014).

[6] A. Hayat, J. P. B. Mueller, and F. Capasso, Lateral chirality-sorting optical forces, Proc. Natl. Acad. Sci. USA **112**, 13190 (2015).

[7] A. Rahimzadegan, M. Fruhnert, R. Alaee, I. Fernandez-Corbaton, and C. Rockstuhl, Optical force and torque on dipolar dual chiral particles, Phys. Rev. B **94**, 125123 (2016).

[8] M. C. Rechtsman, J. M. Zeuner, Y. Plotnik, Y. Lumer, D. Podolsky, F. Dreisow, S. Nolte, M. Segev, and A. Szameit, Photonic floquet topological insulators, Nature (London) **496**, 196 (2013).

[9] S. S. Oh and O. Hess, Chiral metamaterials: Enhancement and control of optical activity and circular dichroism, Nano Convergence **2**, 24 (2015).

[10] V. K. Valev, J. J. Baumberg, C. Sibilia, and T. Verbiest, Chirality and chiroptical effects in plasmonic nanostructures: Fundamentals, recent progress, and outlook, Adv. Mater. **25**, 2517 (2013).

[11] W. Brullot, M. K. Vanbel, T. Swusten, and T. Verbiest, Resolving enantiomers using the optical angular momentum of twisted light, Sci. Adv. **2**, e1501349 (2016).

[12] K. A. Forbes and D. L. Andrews, Optical orbital angular momentum: Twisted light and chirality, Opt. Lett. **43**, 435 (2018).

[13] A. V. Rogacheva, V. A. Fedotov, A. S. Schwanecke, and N. I. Zheludev, Giant Gyrotropy due to Electromagnetic-Field Coupling in a Bilayered Chiral Structure, Phys. Rev. Lett. **97**, 177401 (2006).

[14] Y. Cheng, F. Chen, and H. Luo, Multi-band giant circular dichroism based on conjugated bilayer twisted-semicircle nanostructure at optical frequency, Phys. Lett. A **384**, 126398 (2020).

[15] B. Wang, J. Zhou, T. Koschny, and C. M. Soukoulis, Nonplanar chiral metamaterials with negative index, Appl. Phys. Lett. **94**, 151112 (2009).

[16] M. Saba, M. Thiel, M. D. Turner, S. T. Hyde, M. Gu, K. Grosse-Brauckmann, D. N. Neshev, K. Mecke, and G. E. Schröder-Turk, Circular Dichroism in Biological Photonic Crystals and Cubic Chiral Nets, Phys. Rev. Lett. **106**, 103902 (2011).

[17] C. Kilchoer, N. Abdollahi, J. A. Dolan, D. Abdelrahman, M. Saba, U. Wiesner, U. Steiner, I. Gunkel, and B. D. Wilts, Strong circular dichroism in single gyroid optical metamaterials, Adv. Opt. Mater. **8**, 1902131 (2020).

[18] A. B. Khanikaev, N. Arju, Z. Fan, D. Purtseladze, F. Lu, J. Lee, P. Sarriugarte, M. Schnell, R. Hillenbrand, M. A. Belkin, and G. Shvets, Experimental demonstration of the microscopic origin of circular dichroism in two-dimensional metamaterials, Nat. Commun. **7**, 12045 (2016).

[19] T. Shi, Z.-L. Deng, G. Geng, X. Zeng, Y. Zeng, G. Hu, A. Overvig, J. Li, C.-W. Qiu, A. Alù, Y. S. Kivshar, and X. Li, Planar chiral metasurfaces with maximal and tunable chiroptical response driven by bound states in the continuum, Nat. Commun. **13**, 4111 (2022).

[20] N. Berova, K. Nakanishi, and R. W. Woody, *Circular Dichroism: Principles and Applications* (Wiley, New York, 2000).

[21] A. Micsonai, F. Wien, L. Kernya, Y.-H. Lee, Y. Goto, M. Réfrégiers, and J. Kardos, Accurate secondary structure prediction and fold recognition for circular dichroism spectroscopy, Proc. Natl. Acad. Sci. USA **112**, E3095 (2015).

[22] E. Vinegrad, D. Vestler, A. Ben-Moshe, A. R. Barnea, G. Markovich, and O. Cheshnovsky, Circular dichroism of single particles, ACS Photonics **5**, 2151 (2018).

[23] S. Jia, J. Peng, Y. Cheng, and S. Wang, Chiral discrimination by polarization singularities of a metal sphere, Phys. Rev. A **105**, 033513 (2022).

[24] X. Jiang, Y. Li, B. Liang, J.-c. Cheng, and L. Zhang, Convert Acoustic Resonances to Orbital Angular Momentum, Phys. Rev. Lett. **117**, 034301 (2016).

[25] H. Esfahlani, H. Lissek, and J. R. Mosig, Generation of acoustic helical wavefronts using metasurfaces, Phys. Rev. B **95**, 024312 (2017).

[26] H. Zhou, J. Li, K. Guo, and Z. Guo, Generation of acoustic vortex beams with designed Fermat's spiral diffraction grating, J. Acoust. Soc. Am. **146**, 4237 (2019).

[27] S. Wang, G. Ma, and C. T. Chan, Topological transport of sound mediated by spin-redirection geometric phase, Sci. Adv. **4**, eaaq1475 (2018).

[28] W. Wang, Y. Tan, B. Liang, G. Ma, S. Wang, and J. Cheng, Generalized momentum conservation and Fedorov-Imbert linear shift of acoustic vortex beams at a metasurface, Phys. Rev. B **104**, 174301 (2021).

[29] X.-D. Fan and L. Zhang, Acoustic orbital angular momentum Hall effect and realization using a metasurface, Phys. Rev. Res. **3**, 013251 (2021).

[30] Y. Fu, C. Shen, X. Zhu, J. Li, Y. Liu, S. A. Cummer, and Y. Xu, Sound vortex diffraction via topological charge in phase gradient metagratings, Sci. Adv. **6**, eaba9876 (2020).

[31] Z. Zou, R. Lirette, and L. Zhang, Orbital Angular Momentum Reversal and Asymmetry in Acoustic Vortex Beam Reflection, Phys. Rev. Lett. **125**, 074301 (2020).

[32] Q. Tong and S. Wang, Acoustic helical dichroism in a one-dimensional lattice of chiral resonators, Phys. Rev. B **105**, 024111 (2022).

[33] Z. Y. Hong, J. F. Yin, W. Zhai, N. Yan, W. L. Wang, J. Zhang, and B. W. Drinkwater, Dynamics of levitated objects in acoustic vortex fields, Sci. Rep. **7**, 7093 (2017).

[34] Z. Y. Hong, J. F. Yin, B. W. Zhang, and N. Yan, Vortex-field acoustic levitation in tubes, J. Appl. Phys. **128**, 104901 (2020).

[35] A. Marzo, M. Caleap, and B. W. Drinkwater, Acoustic Virtual Vortices with Tunable Orbital Angular Momentum for Trapping of Mie Particles, Phys. Rev. Lett. **120**, 044301 (2018).

[36] M. Baudoin, J.-C. Gerbedoen, A. Riaud, O. B. Matar, N. Smagin, and J.-L. Thomas, Folding a focalized acoustical vortex on a flat holographic transducer: Miniaturized selective acoustical tweezers, Sci. Adv. **5**, eaav1967 (2019).

[37] W.-C. Lo, C.-H. Fan, Y.-J. Ho, C.-W. Lin, and C.-K. Yeh, Tornado-inspired acoustic vortex tweezer for trapping and manipulating microbubbles, Proc. Natl. Acad. Sci. USA **118**, e2023188118 (2021).

[38] Y. Li, G. Guo, J. Tu, Q. Ma, X. Guo, D. Zhang, and O. A. Sapozhnikov, Acoustic radiation torque of an acoustic-vortex spanner exerted on axisymmetric objects, Appl. Phys. Lett. **112**, 254101 (2018).

[39] R. Wunenburger, J. I. V. Lozano, and E. Brasselet, Acoustic orbital angular momentum transfer to matter by chiral scattering, New J. Phys. **17**, 103022 (2015).

[40] K. Y. Bliokh and F. Nori, Spin and orbital angular momenta of acoustic beams, Phys. Rev. B **99**, 174310 (2019).

[41] Y. Long, D. Zhang, C. Yang, J. Ge, H. Chen, and J. Ren, Realization of acoustic spin transport in metasurface waveguides, Nat. Commun. **11**, 4716 (2020).

[42] S. Wang, G. Zhang, X. Wang, Q. Tong, J. Li, and G. Ma, Spin-orbit interactions of transverse sound, Nat. Commun. **12**, 6125 (2021).

[43] H. Gao, H. Xue, Z. Gu, T. Liu, J. Zhu, and B. Zhang, Non-Hermitian route to higher-order topology in an acoustic crystal, Nat. Commun. **12**, 1888 (2021).

[44] X. Zhang, Y. Tian, J.-H. Jiang, M.-H. Lu, and Y.-F. Chen, Observation of higher-order non-Hermitian skin effect, Nat. Commun. **12**, 5377 (2021).

[45] M. Decker, R. Zhao, C. M. Soukoulis, S. Linden, and M. Wegener, Twisted split-ring-resonator photonic metamaterial with huge optical activity, Opt. Lett. **35**, 1593 (2010).

[46] B. Hopkins, A. N. Poddubny, A. E. Miroshnichenko, and Y. S. Kivshar, Circular dichroism induced by Fano resonances in planar chiral oligomers, Laser Photonics Rev. **10**, 137 (2015).

[47] B. Zhen, C. W. Hsu, Y. Igarashi, L. Lu, I. Kaminer, A. Pick, S.-L. Chua, J. D. Joannopoulos, and M. Soljačić, Spawning rings of exceptional points out of dirac cones, Nature (London) **525**, 354 (2015).

[48] M.-A. Miri and A. Alù, Exceptional points in optics and photonics, Science **363**, eaar7709 (2019).

[49] J. C. W. Lee and C. T. Chan, Polarization gaps in spiral photonic crystals, Opt. Express **13**, 8083 (2005).

[50] T. Christopoulos, O. Tsilipakos, G. Sinatkas, and E. E. Kriezis, On the calculation of the quality factor in contemporary photonic resonant structures, Opt. Express **27**, 14505 (2019).

[51] L. Verslegers, Z. Yu, Z. Ruan, P. B. Catrysse, and S. Fan, From Electromagnetically Induced Transparency to Superscattering with a Single Structure: A Coupled-Mode Theory for Doubly Resonant Structures, Phys. Rev. Lett. **108**, 083902 (2012).

[52] J. Gear, F. Liu, S. T. Chu, S. Rotter, and J. Li, Parity-time symmetry from stacking purely dielectric and magnetic slabs, Phys. Rev. A **91**, 033825 (2015).

[53] J. P. Arenas and M. J. Crocker, Recent trends in porous sound-absorbing materials, Sound Vib. **44**, 12 (2010).

[54] M. Yang and P. Sheng, Sound absorption structures: From porous media to acoustic metamaterials, Annu. Rev. Mater. Res. **47**, 83 (2017).

[55] D. Bothner, S. Yanai, A. Iniguez-Rabago, M. Yuan, Y. M. Blanter, and G. A. Steele, Cavity electromechanics with parametric mechanical driving, Nat. Commun. **11**, 1589 (2020).

[56] H. Nassar, B. Yousefzadeh, R. Fleury, M. Ruzzene, A. Alù, C. Daraio, A. N. Norris, G. Huang, and M. R. Haberman, Nonreciprocity in acoustic and elastic materials, Nat. Rev. Mater. **5**, 667 (2020).

[57] Z. G. Nicolaou and A. E. Motter, Anharmonic classical time crystals: A coresonance pattern formation mechanism, Phys. Rev. Res. **3**, 023106 (2021).